

Large low-field-driven electrocaloric effect in organic-inorganic hybrid TMCM-CdCl₃

Received: 12 October 2024

Accepted: 2 April 2025

Published online: 29 April 2025

Check for updates

Yuan Lin^{1,2,10}, Congcong Chai^{1,3,10}, Zhijie Liu⁴, Jing Wang^{1,2}✉, Shifeng Jin^{1,2}✉, Yurong Yang⁴✉, Yihong Gao^{1,2}, Munan Hao^{1,3}, Xinyue Li^{1,3}, Yuxuan Hou⁵, Xingyue Ma⁴, Bingjie Wang^{1,2}, Zheng Wang^{1,2}, Yue Kan^{1,2}, Jie Zheng^{1,2}, Yang Bai⁵, Yunzhong Chen^{1,2}, Jirong Sun^{1,2,6}, Tongyun Zhao^{1,7}, Jia Yan Law⁸, Victorino Franco⁸✉, Fengxia Hu^{1,2,6}✉ & Baogen Shen^{1,2,7,9}

Due to environmental-friendliness and high-efficiency, electrocaloric effect (ECE) is widely regarded as a refrigeration technology for tomorrow. Herein, utilizing organic-inorganic hybridization strategy, we achieve the largest low-field-driven ECE and highest directly-measured electrocaloric strength (ECS) via packing sphere-like organic cation (CH₃)₃NCH₂Cl⁺ (TMCM⁺) into inorganic one-dimension (1-D) CdCl₃ chain framework. Single-crystal X-ray (SC-XRD) diffraction combined with Raman Spectra reveals that the simultaneous order-disorder transition of organic cations and dramatic structure change of inorganic framework are responsible for the large ECE. Moreover, the measured *P-E* loops and density function theory (DFT) calculations convey that the distinctive electric-field-induced metastable phase and consequential two-step meta-electric transition could lower the transition energy barrier and account for the low driving field. This work shows that the low-symmetry interaction between inorganic framework and organic cations plays a key role in achieving large ECE under low-field, which provides a method for designing high-performance electrocaloric materials via organic-inorganic hybridization.

Refrigeration has become an indispensable part of modern society. However, the dominant vapor compression refrigeration possesses unignorable drawbacks: the low efficiency causes energy waste while the leakage of greenhouse refrigerant exacerbates global warming. Caloric refrigeration, which is based on caloric effects encompassing magnetocaloric, electrocaloric, and mechanocaloric effects^{1–8}, is considered as a promising alternative to vapor compression refrigeration due to its environmental friendliness, high efficiency, and potential of

miniaturization. Caloric effect refers to the isothermal entropy change (ΔS) or adiabatic temperature change (ΔT) driven by an external field. Among these caloric refrigeration, electrocaloric cooling, which harnesses the ubiquitous and cost-effective electric field, is widely regarded as a refrigeration technology for tomorrow.

Since the discovery in the 1930s, the electrocaloric effect (ECE) has garnered enormous attention⁹. Large ECE was first observed in the inorganic ferroelectric ceramic lead zirconate titanate (PbZr_{0.95}Ti_{0.05}O₃)

¹Beijing National Laboratory for Condensed Matter Physics, Institute of Physics, Chinese Academy of Sciences, Beijing, PR China. ²School of Physical Sciences, University of Chinese Academy of Sciences, Beijing, PR China. ³College of Materials Science and Opto-Electronic Technology, University of Chinese Academy of Sciences, Beijing, PR China. ⁴National Laboratory of Solid State Microstructures and Collaborative Innovation Center of Advanced Microstructures, Department of Materials Science and Engineering, Nanjing University, Nanjing, PR China. ⁵Beijing Advanced Innovation Center for Materials Genome Engineering, Institute for Advanced Materials and Technology, University of Science and Technology Beijing, Beijing, PR China. ⁶Songshan Lake Materials Laboratory, Dongguan, Guangdong, PR China. ⁷Ganjiang Innovation Academy, Chinese Academy of Sciences, Ganzhou, Jiangxi, PR China. ⁸Multidisciplinary Unit for Energy Science, Dpto. Física de la Materia Condensada, ICMS-CSIC, Universidad de Sevilla, Sevilla, Spain. ⁹Ningbo Institute of Materials Technology & Engineering, Chinese Academy of Sciences, Ningbo, Zhejiang, PR China. ¹⁰These authors contributed equally: Yuan Lin, Congcong Chai.

✉ e-mail: wangjing@iphy.ac.cn; shifengjin@iphy.ac.cn; yangyr@nju.edu.cn; vfranco@us.es; fxhu@iphy.ac.cn

and organic PVDF-based ferroelectric polymer in 2006 and 2008, respectively^{2,10}. The polar-chain flipping polarization mechanism endows the PVDF-based polymer with a colossal ΔS $\sim 100 \text{ J}\cdot\text{kg}^{-1}\cdot\text{K}^{-1}$ [refs. 2,11] but a high driving field $\sim 100 \text{ MV}\cdot\text{m}^{-1}$, which severely restricts the thickness/mass of refrigerant and thus limits the cooling power¹². Conversely, most ferroelectric perovskite ceramics which derive polarization from ionic displacement typically require a low driving field below $10 \text{ MV}\cdot\text{m}^{-1}$ to induce the disorder-order polarization or the paraelectric-ferroelectric (PE-FE) transition, generating a ΔS lower than $10 \text{ J}\cdot\text{kg}^{-1}\cdot\text{K}^{-1}$ by the reorientation of ionic displacement (relaxor like $\text{PbMg}_{1/3}\text{Nb}_{2/3}\text{O}_3$ - PbTiO_3 ¹³, $\text{PbSc}_{0.5}\text{Ta}_{0.5}\text{O}_3$ ¹⁴, $\text{Na}_{0.5}\text{Bi}_{0.5}\text{TiO}_3$ -based¹⁵, etc.) or mild crystal structure change (first-order transition like BaTiO_3 -based¹⁶). Such a small entropy change hinders their commercial application. Therefore, to obtain an electrocaloric refrigerator with excellent cooling performances, ideal electrocaloric materials (ECMs) should possess a low-field-driven large ECE and a high electrocaloric strength (ECS, defined as $\Delta S/\Delta E$)¹⁶ simultaneously. Unluckily, almost all these organic and inorganic ECMs reported exhibit a small ECS lower than $1 \text{ J}\cdot\text{kg}^{-1}\cdot\text{K}^{-1}\cdot\text{MV}^{-1}\cdot\text{m}$ ^{9,17}, not to mention the requirement of a large ECE accompanied.

Organic-inorganic hybrids, which are commonly designed to combine the specific characteristics of organic and inorganic materials^{18–25}, have shown promising developments in fields of electronics¹⁸, light sources¹⁹, photovoltaics^{20,21}, and ferroelectrics^{22,23}. However, the research on designing ECMs by combining organic and inorganic constituents is at a preliminary stage^{24–28}. On the basis of inorganic perovskites, it is essential to incorporate the inorganic framework to attain a mild driving field. In terms of attaining a large ΔS , the rotation- or the flipping-like motion of the organic molecule should be included. Meanwhile, taking inspiration from the milestone material in the magnetic counterpart, such as giant magnetocaloric materials $\text{Gd}_5\text{Si}_2\text{Ge}_2$ [refs. 29,30] and $\text{La}(\text{Fe}, \text{Si})_{13}$ [ref. 31], a dramatic change of crystal structure may further boost the transition entropy change.

In this work, through packing sphere-like organic cation ($(\text{CH}_3)_3\text{NCH}_2\text{Cl}^+$ (TMCM⁺) into inorganic framework of one-dimension (1-D) CdCl_2 chains, we successfully achieved the largest low-field-driven ECE of $33.1 \text{ J}\cdot\text{kg}^{-1}\cdot\text{K}^{-1}$ @ $7.3 \text{ MV}\cdot\text{m}^{-1}$ and highest directly-measured ECS of $5.64 \text{ J}\cdot\text{kg}^{-1}\cdot\text{K}^{-1}\cdot\text{MV}^{-1}\cdot\text{m}$ in the ferroelectric organic-inorganic hybrid perovskite trimethylchloromethyl ammonium trichlorocadmium ($(\text{CH}_3)_3\text{NCH}_2\text{ClCdCl}_3$ (abbreviated as TMCM- CdCl_3), which is renowned for its excellent piezoelectric performances²³. This result was evidenced by indirect measurements based on P - E loops and quasi-direct, direct measurements based on Differential Scanning Calorimetry (DSC) curves. Single-crystal X-ray diffraction (SC-XRD) combined with Raman spectra showed that during the FE-PE phase transition, dominated by the breaking of Cl-Cl bonds between TMCM⁺ and inorganic chains, crystal symmetry changes from polar space group Cc to centrosymmetric space group $P6_3/mmc$, lattice volume expands by $\sim 1.7\%$, and the fixed TMCM⁺ cation starts to randomly rotate between 12 equivalent orientations. The simultaneous order-disorder transition of the organic cation TMCM⁺ and the dramatic structure change of the inorganic framework can account for the large ECE. Density function theory (DFT) calculations interpreted that due to the low-symmetry interaction imposed by the inorganic framework, the energy barrier of the out-of-plane rotation is larger than that of in-plane rotation for the TMCM⁺ cation, so the external field will first ban the out-of-plane rotation, inducing a metastable phase before totally fixing the cation. Such a field-induced two-step meta-electric transition would effectively reduce the transition energy barrier, leading to the low driving field and thus the high ECS. Our work demonstrates that the organic-inorganic hybridization strategy is conducive to design ideal ECMs with low-field-driven large ECE for refrigeration applications.

Results

Electrocaloric performances

Transparent, colorless, and millimeter-scale TMCM- CdCl_3 single crystals were synthesized at room temperature (see the inset of

Supplementary Fig. S1a). DSC measurement of $1 \text{ K}\cdot\text{min}^{-1}$ showed a phase transition around 400 K , which possesses an overall entropy change of $50 \text{ J}\cdot\text{kg}^{-1}\cdot\text{K}^{-1}$ (Supplementary Fig. S1b) and attractively a small hysteresis of 3.2 K (Supplementary Fig. S1a). P - E loops exhibited the ferroelectricity of the low temperature phase and the paraelectricity of the high-temperature phase (Fig. 1a). Additionally, an S-shape curve, a metamagnetic-transition-like behavior rather than a straight line, appeared at the PE phase near the critical temperature (403 K and 411 K in Fig. 1a, the current switching is shown in Supplementary Note 2). Such a meta-electric transition was once observed in highly ordered $\text{PbSc}_{0.5}\text{Ta}_{0.5}\text{O}_3$ (PST) films³². The appearance of the meta-electric transition means the electric field could trigger the PE-FE transition, indicating an ECE. In ECMs with a first-order FE-PE transition or an antiferroelectric phase, whether there is a meta-electric transition could be adopted as a criterion of the existence of ECE (detailed in Supplementary Note 3). To quantify the ECE, based on the P - E loops and Maxwell relation $(\frac{dP}{dT})_E = (\frac{dS}{dE})_T$, indirect method $\Delta S_{ECE} = \int_0^{E_{\text{max}}} (\frac{\partial P}{\partial T})_E dE$ was applied. Since the electric field was applied along c axis, 36° to the polarization direction (see detailed structure analysis below), the effective electric field should be the component, i.e., $\cos 36^\circ \times E$. Accordingly, an ECE of $36.9 \text{ J}\cdot\text{kg}^{-1}\cdot\text{K}^{-1}$ @ $7.3 \text{ MV}\cdot\text{m}^{-1}$ and an ECS of $7.15 \text{ J}\cdot\text{kg}^{-1}\cdot\text{K}^{-1}\cdot\text{MV}^{-1}\cdot\text{m}$ @ $5.4 \text{ MV}\cdot\text{m}^{-1}$ were achieved around the critical temperature (Fig. 1b). Moreover, with the help of a high-voltage DSC (see Supplementary Note 1 and Fig. S2), quasi-direct and direct measurements were carried out to further investigate the ECE behavior. With different electric fields deployed along c axis, the heat flux at a rate of $10 \text{ K}\cdot\text{min}^{-1}$ was recorded (Supplementary Fig. S3a). Driven by electric field, the critical temperature linearly shifts to high temperatures with a slope of $0.36 \text{ K}\cdot\text{MV}^{-1}$ (Supplementary Fig. S3b). Supplementary Fig. S3d shows the ECE results of quasi-direct measurement. Similarly, an ECE of $34.4 \text{ J}\cdot\text{kg}^{-1}\cdot\text{K}^{-1}$ @ $7.3 \text{ MV}\cdot\text{m}^{-1}$ and an ECS of $6.62 \text{ J}\cdot\text{kg}^{-1}\cdot\text{K}^{-1}\cdot\text{MV}^{-1}\cdot\text{m}$ @ $5.4 \text{ MV}\cdot\text{m}^{-1}$ were observed. Direct measurement was carried out by monitoring the heat flux of the sample at a fixed temperature with the electric field deployed and removed (Supplementary Fig. S4)^{33,34}. Figure 1c presents the entropy change of the exothermic peak and compares the ECE data obtained via different measurements. An ECS of $5.64 \text{ J}\cdot\text{kg}^{-1}\cdot\text{K}^{-1}\cdot\text{MV}^{-1}\cdot\text{m}$ and an ECE of $33.1 \text{ J}\cdot\text{kg}^{-1}\cdot\text{K}^{-1}$ @ $7.3 \text{ MV}\cdot\text{m}^{-1}$ were observed via direct measurement. One can see that the ECE resulting from different methods fits well with each other.

Figure 1d, e compares the electrocaloric properties of the presented material with others. Almost all the ECMs possess a small ECS below $1 \text{ J}\cdot\text{kg}^{-1}\cdot\text{K}^{-1}\cdot\text{MV}^{-1}\cdot\text{m}$. Few inorganic perovskites like BaTiO_3 and the recently reported ImClO_4 own a high ECS surpassing $1 \text{ J}\cdot\text{kg}^{-1}\cdot\text{K}^{-1}\cdot\text{MV}^{-1}\cdot\text{m}$ ^{16,25}, but a small ECE of $\sim 5 \text{ J}\cdot\text{kg}^{-1}\cdot\text{K}^{-1}$, while, in contrast, the well-tailored organic PVDF polymer possesses a large ECE but a small ECS of $\sim 1 \text{ J}\cdot\text{kg}^{-1}\cdot\text{K}^{-1}\cdot\text{MV}^{-1}\cdot\text{m}$ (Fig. 1d)^{4,6}. Comparatively, the presented hybrid perovskite simultaneously shows a high ECS of $5.64 \text{ J}\cdot\text{kg}^{-1}\cdot\text{K}^{-1}\cdot\text{MV}^{-1}\cdot\text{m}$ and a large ECE of $33.1 \text{ J}\cdot\text{kg}^{-1}\cdot\text{K}^{-1}$. Figure 1e illustrates that, when operated at a low electric field, most reported ECMs exhibit an ECE below $5 \text{ J}\cdot\text{kg}^{-1}\cdot\text{K}^{-1}$. In comparison, the presented material demonstrates a ΔS that is 5–10 times larger than most ECMs at a low operating field. Relative Cooling Power (RCP) defined as $\Delta S_{\text{peak}} \times \delta T_{\text{FWHM}}$, where ΔS_{peak} denotes the peak value of entropy change and δT_{FWHM} denotes the full width at half maximum (FWHM), is commonly used to quantify the cooling capacity of caloric materials (Supplementary Note 6)³. The RCP of the presented material is $245 \text{ J}\cdot\text{kg}^{-1}$ @ $7.3 \text{ MV}\cdot\text{m}^{-1}$. However, for most ECMs with broad but shallow peaks, RCP cannot predict their cooling capacity accurately. Therefore, another figure of merit called Temperature Averaged Entropy Change (TEC)³⁵ is widely accepted to evaluate the actual cooling capacity: $\text{TEC}(T_{\text{lift}}) = \frac{1}{T_{\text{lift}}} \max\left\{\int_{T_{\text{mid}} - \frac{T_{\text{lift}}}{2}}^{T_{\text{mid}} + \frac{T_{\text{lift}}}{2}} \Delta S(T)_{\Delta E} dT\right\}$, where T_{lift} is the temperature span that refrigerators could actually reach

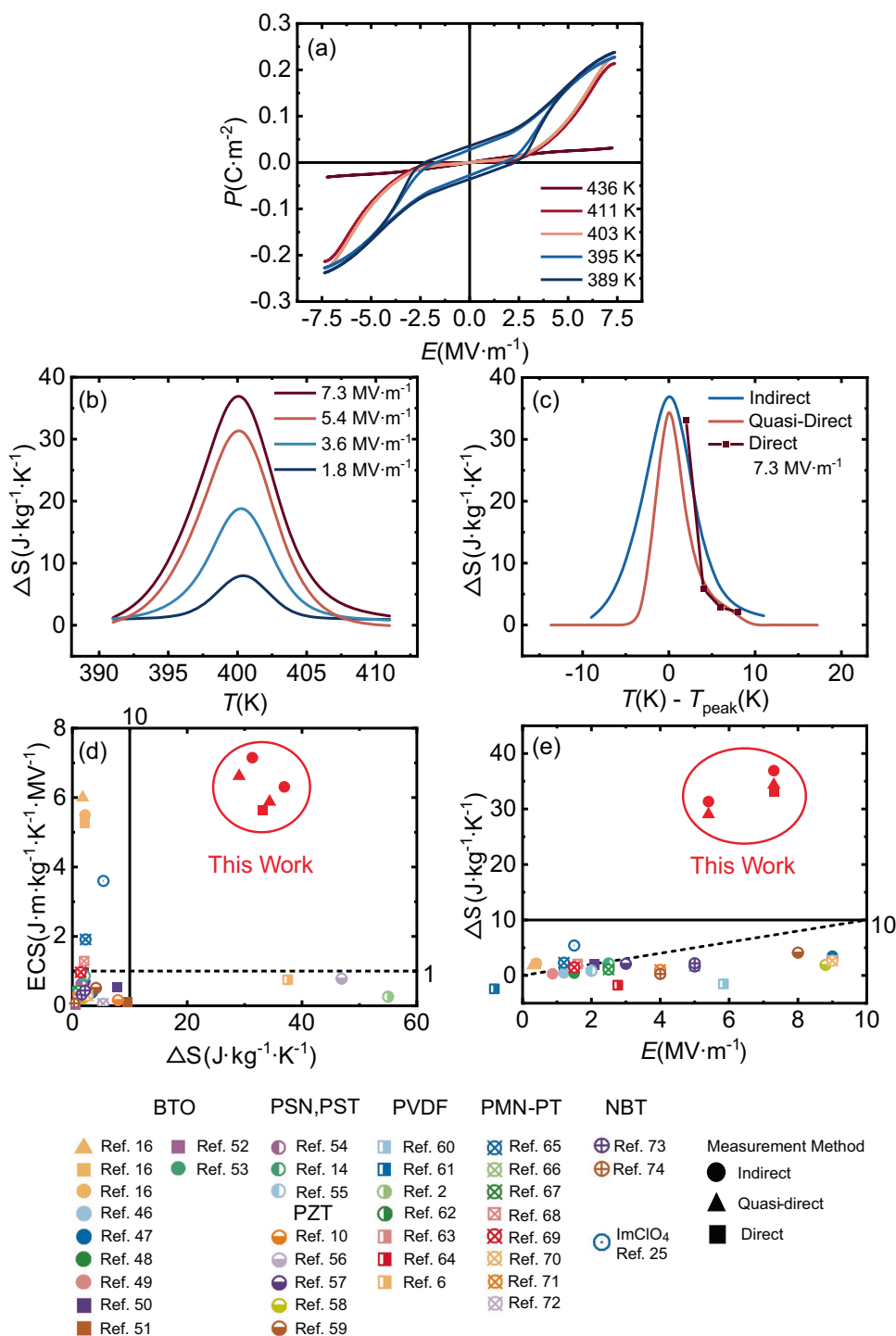


Fig. 1 | Indirect, quasi-direct, and direct measurements of the ECE of (001) TMCm-CdCl₃ single crystals. **a** P - E loops of the single crystal where the polarization and electric field are along c axis. **b** The ECE obtained by indirect measurement based on the P - E loops in (a). **c** The comparison of the ECE obtained by different measurements. The electric field is applied along c axis. The comparison

of electrocaloric properties between the presented material and others. **d** The ECS and ΔS . **e** The ΔS and its driving electric field. The materials include BTO, PVDF, PZT(PbZrTiO), PST(PbScTaO), PSN(PbScNbO), PMN-PT, NBT(NaBiTiO), ImClO₄ and this work. The solid line denotes the entropy change of $10 \text{ J} \cdot \text{kg}^{-1} \cdot \text{K}^{-1}$ and the dashed line denotes the ECS of $1 \text{ J} \cdot \text{kg}^{-1} \cdot \text{K}^{-1} \cdot \text{MV}^{-1} \cdot \text{m}^2$.^{2,6,10,14,16,25,46-74}

(Supplementary Note 6). Selecting T_{lift} as 10 K, the TEC(10) of the presented material is $24.1 \text{ J} \cdot \text{kg}^{-1} \cdot \text{K}^{-1}$ @ $7.3 \text{ MV} \cdot \text{m}^{-1}$, which is 5 times larger than the high-performance PST film of $4.8 \text{ J} \cdot \text{kg}^{-1} \cdot \text{K}^{-1}$ @ $15.8 \text{ MV} \cdot \text{m}^{-1}$ recently reported³². Since PVDF polymers cannot be activated at low driving fields, as far as we know, the presented material shows the largest TEC(10) of ECMs at low operating fields. Thereby, the class of organic-inorganic hybrid ferroelectrics may be a good candidate for caloric refrigeration.

Crystal structure: origin of the large ECE

To understand the origin of the large entropy change, SC-XRD was performed to acquire structure information. The results suggest that the crystal undergoes a dramatic change of crystal symmetry from polar space group Cc to centrosymmetric space group $P6_3/mmc$ (Fig. 2) across the FE-PE phase transition around 400 K and an accompanying volume expansion of -1.7% (see Supplementary Fig. S20 and Supplementary Table S1). The corresponding lattice relation

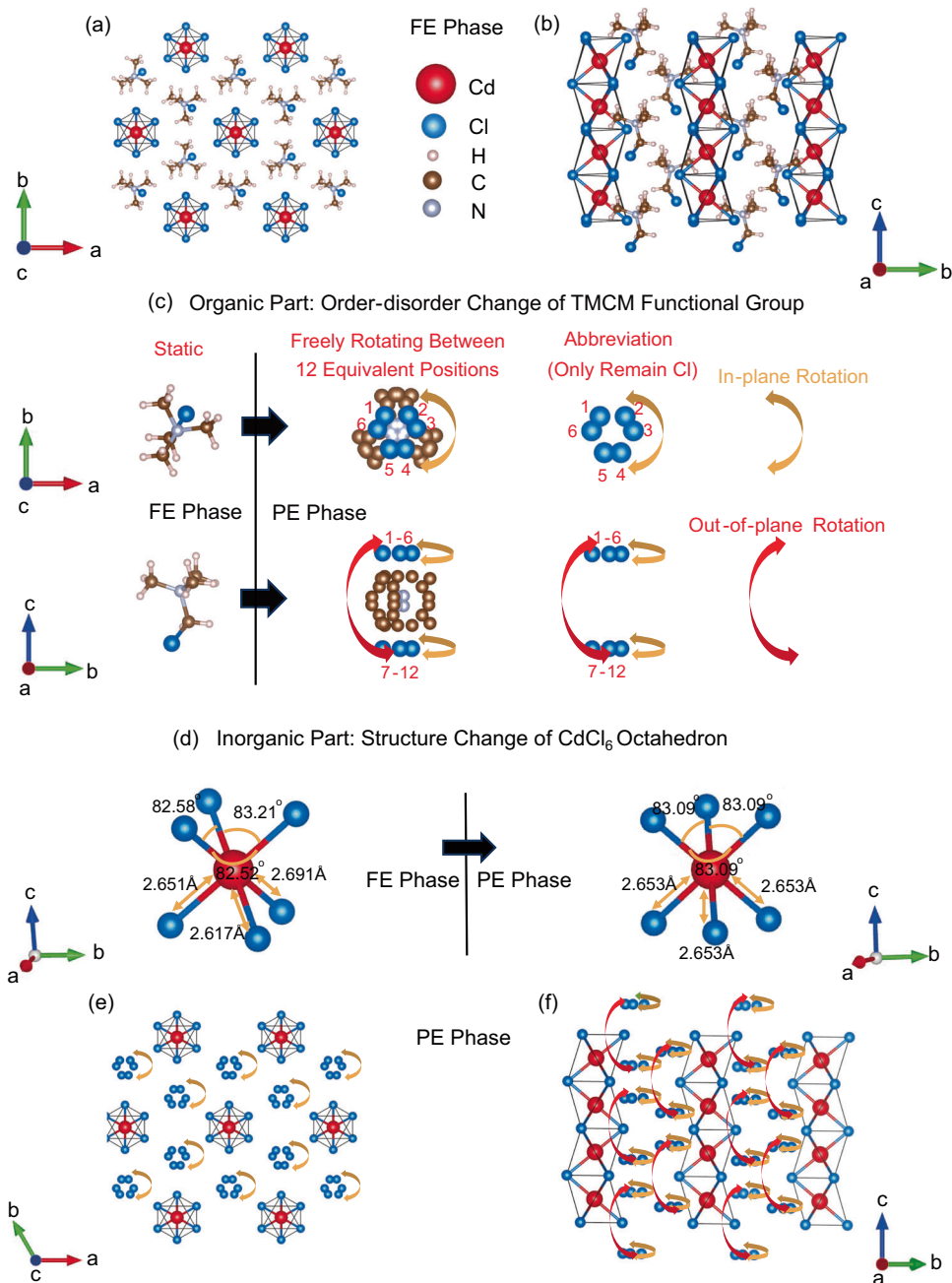


Fig. 2 | The crystalline structure information of TMCM- CdCl_3 provided by SC-XRD. At the FE phase, the crystal structure observed from the (a) c_L and b_{a_L} axis, in which the organic cation TMCM^+ is fixed at one specific orientation (fixed). c The schematic of the order-disorder (fixed–freely rotating) change of the organic

cation. d The schematic of the structure change of the inorganic CdCl_6 octahedron. At the PE phase, the crystal structure observed from the (e) c_H and f_{a_H} axis, in which the organic cation tumbles randomly between 12 equivalent orientations (freely rotating). C, H, and N atoms are omitted at the PE phase.

between the two phases can be expressed as follows: $\mathbf{a}_L \approx \mathbf{a}_H$, $\mathbf{b}_L = \mathbf{a}_H + 2\mathbf{b}_H$, $\mathbf{c}_L = \mathbf{c}_H$ (Supplementary Fig. S21). Figure 2 depicts the crystal structure composed of 1-D inorganic CdCl_3 chains and sphere-like organic TMCM^+ cations. Being parallel along c axis, these chains are spaced evenly in the ab plane and stabilized by interchain van der Waals (vdW) force, while organic cations are imprisoned within the space between the chains (Fig. 2a, b, e, f and Supplementary Fig. S22). Specifically, connected with three joint Cl atoms, CdCl_6 octahedrons zigzag along c axis, constructing the 1-D inorganic chain (Fig. 2b, f). The organic cation $(\text{CH}_3)_3\text{NCH}_2\text{Cl}^+$, formed by substituting a H atom in $(\text{CH}_3)_4\text{N}$ with a Cl atom (Fig. 2c), is fixed at a specific direction and links tightly to the inorganic chain through Cl–Cl halogen bonds at the FE phase (Fig. 2a, b). The refinement results show that at the FE phase, the

CdCl_6 octahedron distorts: the length of the three Cd–Cl bonds and the angle of the three Cl–Cd–Cl bond angles in the same octahedron are different due to the stretching of Cl–Cl bonds (Fig. 2d and Supplementary Fig. S24), while in the high-temperature PE phase, the distortion disappears and the Cd–Cl bond length and Cl–Cd–Cl bond angles turn to be the same (Fig. 2d and Supplementary Fig. S24). Besides, during the FE–PE transition, b expands about 1.8%, which means that the distance between the adjacent inorganic chains along b axis increases (Supplementary Figs. S20b and S26), so the imprisoning force posed to the organic cation is weakened. As a result, thermal agitation is able to overcome the energy barrier formed by Cl–Cl bonds between TMCM^+ and inorganic chains and drives the organic cations to rotate randomly among 12 equivalent positions (Fig. 2c, e, f and

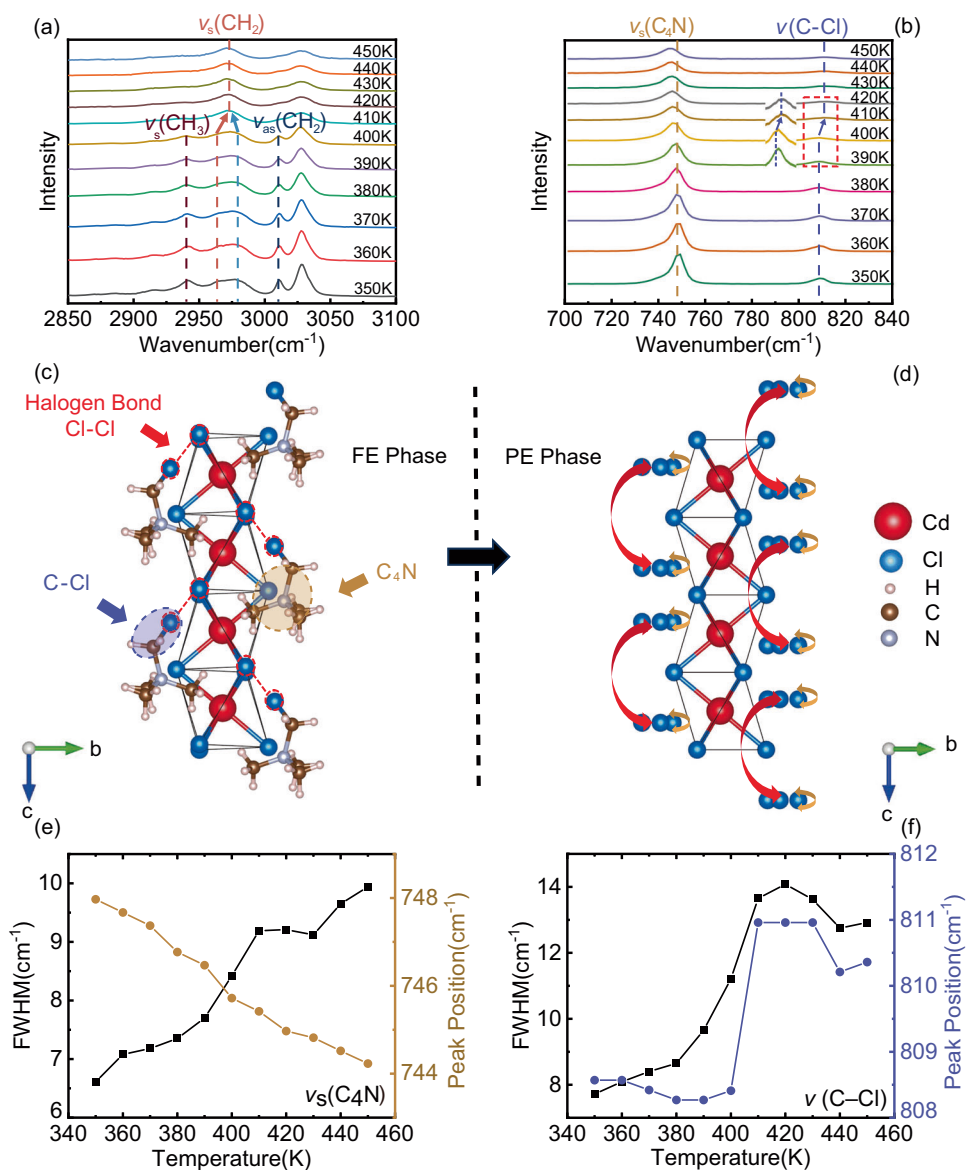


Fig. 3 | Raman spectra and structure information of TMCM-CdCl₃. Raman spectra in the region of (a) 2850–3100 cm⁻¹ and (b) 700–840 cm⁻¹ at different temperatures around the FE-PE transition. The inset of (b) is the enlargement of the blueshift of $\nu(\text{C-Cl})$. (c) At the FE phase, the crystal structure viewed along a_L . The dashed red line denotes the Cl-Cl bond fixing the organic cation and the red circle

marks the related Cl atoms. The purple circle denotes the C-Cl bond and the brown circle denotes the C₄N molecular group. (d) At the PE phase, the crystal structure viewed along a_H . The FWHM and wavenumber of (e) the C₄N stretching vibration and (f) C-Cl stretching vibration as a function of temperature.

Supplementary Fig. S22c, d) involving six in-plane equivalent positions (Fig. 2c, e) and two out-of-plane equivalent positions (Fig. 2c, f). Raman spectra were conducted to gain further insights into the structure (Fig. 3 and Supplementary Note 9).

Figure 3a, b displays the Raman spectra region of 2850–3100 cm⁻¹ and 700–840 cm⁻¹ at different temperatures around the FE-PE transition respectively³⁶. As shown in Fig. 3a, the disappearance of the stretching mode $\nu_s(\text{CH}_3)$, $\nu_{as}(\text{CH}_2)$, and the collapse of $\nu_s(\text{CH}_2)$ imply the increase of structure symmetry and the weakening of interchain connection, vdW force^{37,38} (see Supplementary Note 9 for more details). According to SC-XRD, the crystal symmetry increases from Cc to P6₃/mmc, and b expands about 1.8% (Supplementary Fig. S20b) during the FE-PE transition, which means the distance between the adjacent inorganic chains along b axis is elongated (Supplementary Fig. S26), consequently weakening the interchain vdW force.

Figure 3e, f shows the FWHM and the wavenumber of C₄N, C-Cl stretching vibration modes extracted from Fig. 3b. Commonly, FWHM

is closely related to the phonon's lifetime, which is highly dependent on structural disorder³⁹. The strong discontinuity and broadening of the FWHM across the transition for both modes imply the increase of structure disorder during the FE-PE transition (Fig. 3e, f). The abnormal blueshift, i.e., the sudden frequency increase of the $\nu(\text{C-Cl})$ at around 808 cm⁻¹ implies that the Cl atom in TMCM⁺ suddenly becomes less limited and more free (Fig. 3f). This also manifests that the intramolecular bonding C-Cl in TMCM⁺ is hardened and the intermolecular bonding between TMCM⁺ and inorganic chains is weakened after the transition, suggesting the breaking of the Cl-Cl bonds connecting organic-inorganic parts during the transition (Fig. 3c, d). As a result, the drag force between the inorganic chain and the TMCM⁺ recedes, so the TMCM⁺ cation releases and the $\nu_s(\text{C}_4\text{N})$ vibration frequency around 746 cm⁻¹ decreases (Fig. 3e). In summary, at the FE phase, via the drag of Cl-Cl halogen bonds, the organic cation is ordered and the CdCl₆ octahedron distorts, which induces the ion displacement between the

inorganic framework and the organic cation and thus spontaneous polarization (detailed in Supplementary Note 8)^{23,40}. There are six equivalent polarization directions for $\mathbf{P}_{x,y}$ component (Supplementary Fig. S28) and two equivalent polarization directions for \mathbf{P}_z component (Supplementary Fig. S29). Uncommonly, there are 12 spontaneous polarization directions in total whose angle to the c axis (001) is about 36° (Supplementary Figs. S28–S30)^{23,40}. At the PE phase, after the Cl–Cl bonds break, the organic cation is disordered, the distortion disappears, and thus the spontaneous polarization vanishes. The ferroelectric mechanism of the presented material is an order-disorder type rather than a displacive type. Though both organic and inorganic parts change obviously during the transition, the ferroelectric spontaneous polarization and domain switching energy barrier mainly come from the organic part (see Supplementary Table S3 and Supplementary Note 10). Accompanying the breaking of Cl–Cl bonds, the release of TMCM⁺ rotation degree together with the change of inorganic CdCl₆ framework structure account for the large entropy change during the FE–PE transition, while the strong electro-structural coupling enables the large entropy change to be utilized by electric field, thereby producing large ECE.

DFT calculations: origin of the low driving field

To comprehend the underlying mechanism of the low driving field and the meta-electric transition, i.e., the S -shape P - E loop (Fig. 1a), DFT calculations were carried out (detailed in Supplementary Note 11). A supercell with two TMCM⁺ cations was considered (detailed in Supplementary Note 8). The energy of the structure with one TMCM⁺ fixed at a specific orientation and the other rotating gradually from 0° to 360° was calculated (See Supplementary Movies 1 and 2). The energy barrier for the in-plane rotation of TMCM⁺ is about 450 meV (Fig. 4a and Supplementary Table S2) and that for out-of-plane is about 600 meV (Fig. 4b), indicating it is easier for TMCM⁺ cations to rotate in-plane. The difference is caused by the low-symmetry interaction between the 1-D CdCl₃ chain cage and imprisoned TMCM⁺ cations. The rigidity renders the inorganic chains difficult to distort, so the restriction to the movement of TMCM⁺ perpendicular to the 1-D chains is more strict. Compared to the in-plane rotation (Supplementary Movie 1), the out-of-plane rotation (Supplementary Movie 2) needs to buckle the 1-D chains, thus possessing a larger energy barrier. With an electric field applied along the 1-D chain, the energy barrier of the out-of-plane rotation affected by electrostatic potential energy would be enlarged (Supplementary Fig. S37). When the electric field is small, the TMCM⁺ cations can still tumble between the 12 equivalent orientations (freely rotating), so the P - E loop along c axis exhibits a traditional PE linear behavior (Fig. 4d, h and the PE phase in Fig. 4k). At the same time, there is no in-plane polarization (PE phase in Fig. 4l). With electric field increasing and energy barriers enlarged, the out-of-plane rotation will first be banned while the in-plane rotation is still permitted (restrictedly rotating) (Fig. 4e, i), leading to the formation of the long-range order along c axis and the surge of out-of-plane polarization in P - E loops (403 K and 411 K in Fig. 1a, the metastable phase in Fig. 4k). Meanwhile, since the in-plane rotation is permitted, there is still no in-plane polarization (the metastable phase in Fig. 4l). Such metastable phase resembles the FE ground phase observed in TMCM-CdBr₃ with similar structural properties⁴¹. With the electric field further increasing, the crystal turns to the full FE phase and the in-plane rotation is also limited (fixed) (Fig. 4f, j). The out-of-plane polarization has approached to saturation at the metastable phase, so it does not change much during the transition from the metastable phase to the FE phase (the FE phase in Fig. 4k), while since the in-plane rotation is banned, a long-range order forms in the ab plane, and there is a surge of the in-plane polarization (the FE phase in Fig. 4l). As temperature increases, the critical field inducing the metastable phase increases, and when the temperature is high enough, the long-range order is broken by thermal

agitation and the P - E loop is linear again (436 K in Fig. 1a). The low-symmetry interaction caused metastable phase breaks the field-induced PE–FE transition into two steps, hence decreasing the transition energy barrier and effectively lowering the driving field.

Discussion

The low-symmetry interaction between the inorganic framework and organic cations plays a crucial role in realizing large ECE under low driving field. In the presented material, each TMCM⁺ cation is imprisoned in a narrow regular triangular prism formed by three surrounding inorganic chains (Fig. 2 and Supplementary Note 8). The imprisoning force posed to the cation has a low symmetry of $3/m$ (Supplementary Fig. S38). Due to this low-symmetry interaction, it is more difficult for TMCM⁺ cations to turn over than to turn around in the narrow prism cage, i.e., different rotation freedom possesses distinct excitation energy, which creates conditions for the stepwise transition. If imprisoned in a cubic cage with high-symmetry interaction like $m\bar{3}m$, the excitation energy for different rotation freedom would be similar, where the stepwise transition may disappear. Generally, one may expect that the excitation energy for various freedom of motion of the organic functional group would be different for organic-inorganic hybrids in which the inorganic framework provides a low-symmetry interaction. Under the combined influence of the interaction and electric field, different freedoms of motion will be banned stepwise, and many interesting metastable phases with novel physical properties will emerge. As a result, the intact one-step PE–FE transition would be taken apart into several steps, thus lowering the transition energy barrier and driving field (Supplementary Fig. S39). Through the low-symmetry interaction, the inorganic framework could intensify the influence of the electric field on the organic functional group, freezing the freedom at a low field and thus facilitating a low-field-driven ECE.

To conclude, a low-field-driven large ECE of $33.1\text{ J}\cdot\text{kg}^{-1}\cdot\text{K}^{-1}$ @ $7.3\text{ MV}\cdot\text{m}^{-1}$ and a high ECS of $5.64\text{ J}\cdot\text{kg}^{-1}\cdot\text{K}^{-1}\cdot\text{MV}^{-1}\cdot\text{m}$ were demonstrated in organic-inorganic hybrid TMCM-CdCl₃ perovskites. SC-XRD combined with Raman spectra revealed that accompanying the dramatic structure change of the inorganic framework, the initially fixed TMCM⁺ cations in the FE phase become tumbling between 12 orientations with the breaking of Cl–Cl bonds connecting organic-inorganic parts. These synergistical changes in the rotation-disordering of organic TMCM⁺ and the inorganic CdCl₃ framework give rise to the large ECE. Moreover, DFT calculations revealed that the low-symmetry interaction between the inorganic framework and organic cations breaks the electric-field-induced TMCM⁺ disorder-order transition with a large entropy change into two steps, resulting in a distinctive electric-field-induced two-step meta-electric transition, thus reducing the driving field effectively and enabling the high ECS and low-field-driven large ECE in the presented TMCM-CdCl₃. By selecting an organic group with larger configuration entropy and correspondingly tailoring the low-symmetry interaction force, ECMs with more excellent performance could be designed in the future. Our work opens the possibility of designing ideal ECMs with low-field-driven large ECE through the organic-inorganic hybridization strategy, highlighting the immense potential of hybrid materials in the field of electrocaloric refrigeration.

Methods

Sample preparation

Trimethylamine (33 wt% in ethanol), dichloromethane (99.9% pure), and CdCl₂ (99% pure) were bought from Innochem. (Chloromethyl) trimethylammonium chloride (TMCMCl) was synthesized according to the method reported in the ref. 23 by the reaction of equimolar amounts of trimethylamine (33 wt% in ethanol) and dichloromethane (99.9% pure) in tetrahydrofuran at room temperature for 24 h²³. The solvent was removed in the vacuum oven. The obtained colorless solid TMCMCl is hygroscopic and placed in a vacuum desiccator. TMCMCl

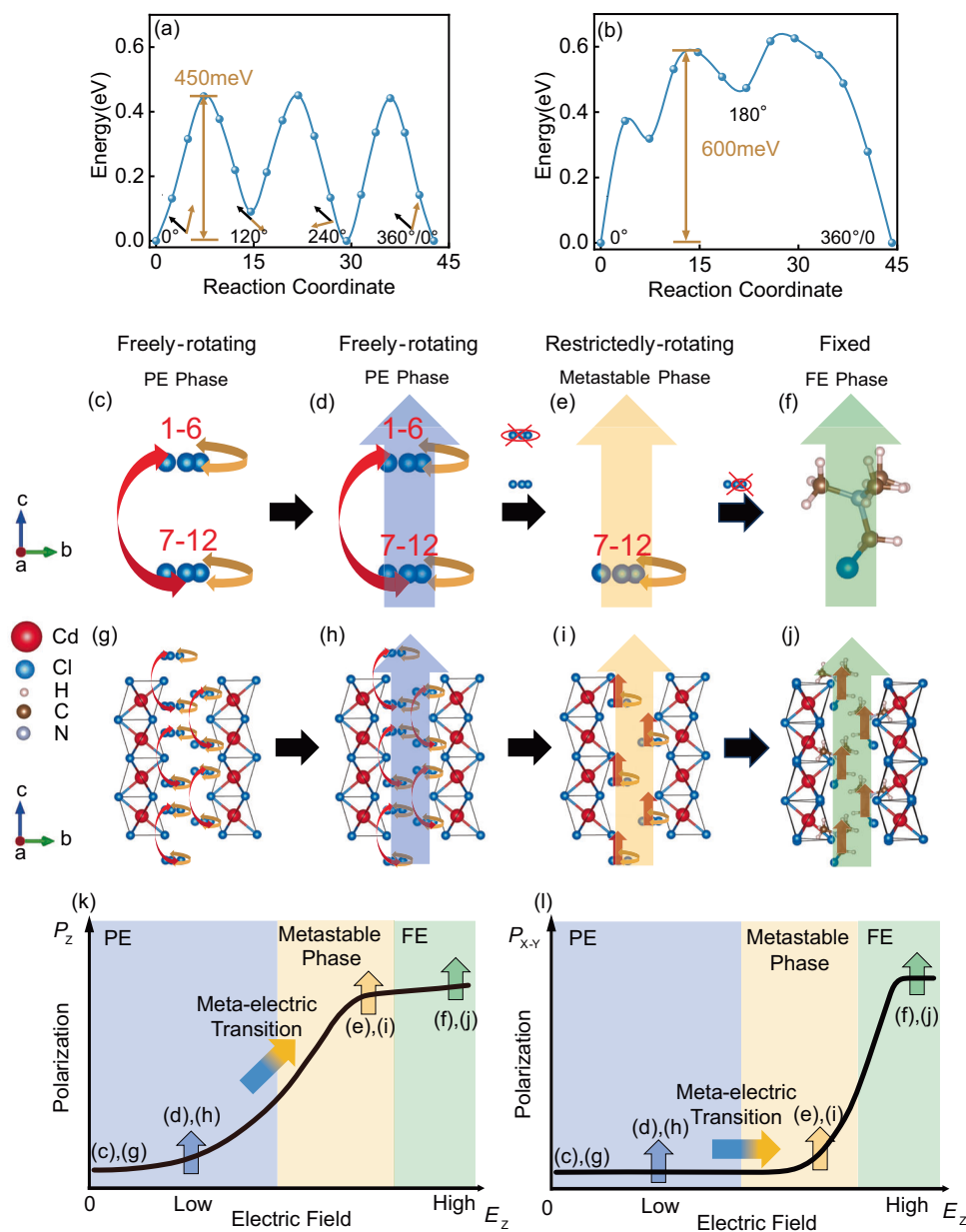


Fig. 4 | DFT computations of the energy barriers of TMCM⁺ rotation. The supercell energy as a function of (a) TMCM⁺ in-plane rotation and b TMCM⁺ out-of-plane rotation. c–f, g–j show evolution of the organic cations and the crystal structure from the PE phase (freely rotating) to the metastable phase (restrictedly rotating) and finally to the FE phase (fixed) viewed along d_H . The black and yellow

arrows in (a) denote the in-plane polarization direction of the two TMCM⁺ cations. With electric field applied along c axis, the (k) out-of-plane polarization (P_z) and l in-plane polarization ($P_{x,y}$) as a function of electric field. Note that the applied electric field is parallel to the out-of-plane polarization but perpendicular to the in-plane polarization. Thus, (k) is also the schematic of the P - E loops along c axis.

and CdCl₂ (99 % pure) at equal stoichiometric ratio were dissolved in deionized water, and the solutions were then filtered by a 0.22 μm filter after the reactants had reacted sufficiently. The colorless crystals up to 5 mm were obtained by slow evaporation of the aqueous solution at room temperature.

High resolution SC-XRD

SC-XRD data were collected using a Rigaku XtaLAB PRO 007HF diffractometer at different temperatures. The sources were multilayer monochromatized Mo $K\alpha$ radiation ($\lambda = 0.71073 \text{ \AA}$). Data collection, cell refinement, and data reduction were carried out in the CryAlisPro system, and the data were solved by intrinsic phasing methods and refined by the full-matrix method based on F^2 using the SHELXT software package⁴².

Raman spectra

The Raman spectra were collected on a Raman spectrometer (Lab RAM HR Evolution) at the Synergetic Extreme Condition User Facility (SECUF). The (001) single crystal was attached to the sample puck. Before measurement, a 50X objective lens was used to adjust the position of the sample. After that, the sample puck was vacuumized by a mechanical pump and a molecular pump in order. The temperature of the sample was controlled by a cryostat (Oxford MHI). The wavelength of the laser source is 532 nm, and to avoid damaging the sample, the intensity of the laser was set to 5%. Full Raman spectra from 100 cm⁻¹ to 3500 cm⁻¹ were collected at variable temperature from 350 K to 450 K upon heating. To ensure complete thermalization, when reaching the target temperature, the sample was kept for another 5 min before data collection. To reduce the effect of noise,

each full spectrum was collected 5 times. The data collection lasted 10 s each time.

DSC measurements

The heat flux curves under zero electric field were measured by a commercial DSC (NETZSCH DSC 214 SET MFC LN2), where liquid N₂ was employed to control temperature. According to the standard calibration process in the manual, melting enthalpy of the six prescribed standard samples was measured to ensure the accuracy of the measured latent heat of phase transition before measurement: C₁₀H₁₆ (9.015 g, -208.7 K, -22 J·g⁻¹, 99.9999% pure), In (10.519 g, 429.8 K, -28.6 J·g⁻¹, 99.9999% pure), Sn (12.577 g, 505.1 K, -60.5 J·g⁻¹, 99.9999% pure), Bi (9.858 g, 544.6 K, -53.3 J·g⁻¹, 99.9999% pure), Zn (10.196 g, 692.7 K, -107.5 J·g⁻¹, 99.9999% pure), and CsCl (11.042 g, 749.2 K, -17.22 J·g⁻¹, 99.9999% pure).

The quasi-direct and direct measurements of ECE were also carried out on the commercial DSC (NETZSCH DSC 214 SET MFC LN2), where a DC power supply was applied to provide different electric fields. (001) single crystals of 0.22 mm were glued to the Al₂O₃ crucible with silver epoxy to guarantee good thermal contact and optimal conductivity. The upper surface of the sample was also covered with silver epoxy. Two wires were connected to the inside bottom of the crucible and the upper surface of the sample. The other end of the wires was connected to the DC power supply. Besides standard calibration, an additional calibration was conducted (detailed in Supplementary Note 1)^{33,34}.

P-E loops

The P-E loops were obtained via a FE measuring system (aixACCT TF Analyzer 2000). Both surfaces of the (001) single crystal sample of 0.22 mm were covered by silver epoxy to guarantee optimal conductivity. The P-E loops were collected upon heating. Similarly, the sample stayed for 5 min at each temperature point to ensure complete thermalization before data collection. To exclude the influence of the nonequilibrium process, instead of the lower branch, the upper branch was applied to calculate the ECE via the Maxwell equation.

DFT computation

Our DFT calculations were performed via the Vienna ab initio simulation package⁴³. We used generalized gradient approximation by Perdew, Burke, and Ernzerhof for solids (GGA-PBEsol) and the projected augmented wave pseudopotentials to relax structures. The Monkhorst-Pack k-meshes⁴⁴ were set to 3 × 3 × 4 in the Brillouin zone and the energy cutoff of 550 eV was used for all calculations. The residual forces were below 0.005 eV·Å⁻¹ on each atom to be converged. Cd 5s²4d¹⁰, Cl 3s²3p⁵, N 2s²2p³, C 2s²2p², and H 1s¹ were treated as valence electrons. The energy barrier of the phase transition was calculated by a generalized solid-state nudged elastic band method⁴⁵.

Data availability

Relevant data supporting the key findings of this study are available within the paper and its Supplementary Information. All raw data generated during the current study are available from the corresponding author (F.H.) upon request.

References

- Moya, X. & Mathur, N. D. Caloric materials for cooling and heating. *Science* **370**, 797–803 (2020).
- Neese, B. et al. Large electrocaloric effect in ferroelectric polymers near room temperature. *Science* **321**, 821–823 (2008).
- Franco, V. et al. Magnetocaloric effect: from materials research to refrigeration devices. *Prog. Mater. Sci.* **93**, 112–232 (2018).
- Zheng, S. et al. Colossal electrocaloric effect in an interface-augmented ferroelectric polymer. *Science* **382**, 1020–1026 (2023).
- Ma, R. et al. Highly efficient electrocaloric cooling with electrostatic actuation. *Science* **357**, 1130–1134 (2017).
- Qian, X. et al. High-entropy polymer produces a giant electrocaloric effect at low fields. *Nature* **600**, 664–669 (2021).
- Takeuchi, I. & Sandeman, K. Solid-state cooling with caloric materials. *Phys. Today* **68**, 48–54 (2015).
- Manosa, L., Planes, A. & Acet, M. Advanced materials for solid-state refrigeration. *J. Mater. Chem. A* **1**, 4925–4936 (2013).
- Barman, A., Kar-Narayan, S. & Mukherjee, D. Caloric effects in perovskite oxides. *Adv. Mater. Interfaces* **6**, 1900291 (2019).
- Mischenko, A. S., Zhang, Q., Scott, J. F., Whatmore, R. W. & Mathur, N. D. Giant electrocaloric effect in thin-film PbZr_{0.95}Ti_{0.05}O₃. *Science* **311**, 1270–1271 (2006).
- Chu, B. et al. A dielectric polymer with high electric energy density and fast discharge speed. *Science* **313**, 334–336 (2006).
- Cai, Y. et al. Polymeric nanocomposites for electrocaloric refrigeration. *Front. Energy* **17**, 450–462 (2023).
- Bai, Y., Wei, D. & Qiao, L.-J. Control multiple electrocaloric effect peak in Pb(Mg_{1/3}Nb_{2/3})O₃-PbTiO₃ by phase composition and crystal orientation. *Appl. Phys. Lett.* **107**, 192904 (2015).
- Shebanov, L. & Borman, K. On lead-scandium tantalate solid-solutions with high electrocaloric effect. *Ferroelectrics* **127**, 143–148 (1992).
- Cao, W. P. et al. Large electrocaloric response and high energy-storage properties over a broad temperature range in lead-free NBT-ST ceramics. *J. Eur. Ceram. Soc.* **36**, 593–600 (2016).
- Moya, X. et al. Giant electrocaloric strength in single-crystal BaTiO₃. *Adv. Mater.* **25**, 1360–1365 (2013).
- Shi, J. et al. Electrocaloric cooling materials and devices for zero-global-warming-potential, high-efficiency refrigeration. *Joule* **3**, 1200–1225 (2019).
- Mitzi, D. B., Feild, C. A., Harrison, W. T. A. & Guloy, A. M. Conducting tin halides with a layered organic-based perovskite structure. *Nature* **369**, 467–469 (1994).
- Cho, H. et al. Overcoming the electroluminescence efficiency limitations of perovskite light-emitting diodes. *Science* **350**, 1222–1225 (2015).
- Hao, F., Stoumpos, C. C., Duyen Hanh, C., Chang, R. P. H. & Kanatzidis, M. G. Lead-free solid-state organic-inorganic halide perovskite solar cells. *Nat. Photonics* **8**, 489–494 (2014).
- Tsai, H. et al. High-efficiency two-dimensional Ruddlesden-Popper perovskite solar cells. *Nature* **536**, 312–316 (2016).
- Ye, H.-Y. et al. Bandgap engineering of lead-halide perovskite-type ferroelectrics. *Adv. Mater.* **28**, 2579–2586 (2016).
- You, Y.-M. et al. An organic-inorganic perovskite ferroelectric with large piezoelectric response. *Science* **357**, 306–309 (2017).
- Li, P.-F. et al. Unprecedented ferroelectric-antiferroelectric-paraelectric phase transitions discovered in an organic-inorganic hybrid perovskite. *J. Am. Chem. Soc.* **139**, 8752–8757 (2017).
- Li, W. et al. The strong electrocaloric effect in molecular ferroelectric ImClO₄ with ultrahigh electrocaloric strength. *J. Mater. Chem. A* **8**, 16189–16194 (2020).
- Liu, X. et al. Giant room temperature electrocaloric effect in a layered hybrid perovskite ferroelectric: [(CH₃)₂CHCH₂NH₃]₂PbCl₄. *Nat. Commun.* **12**, 5502 (2021).
- Li, M. et al. Soft perovskite-type antiferroelectric with giant electrocaloric strength near room temperature. *J. Am. Chem. Soc.* **142**, 20744–20751 (2020).
- Han, S. et al. Field-induced antiferroelectric-ferroelectric transformation in organometallic perovskite displaying giant negative electrocaloric effect. *J. Am. Chem. Soc.* **146**, 8298–8307 (2024).
- Pecharsky, V. K. & Gschneidner, K. A. Giant magnetocaloric effect in Gd₅(Si₂Ge₂). *Phys. Rev. Lett.* **78**, 4494–4497 (1997).
- Pecharsky, V. K. & Gschneidner, K. A. Tunable magnetic regenerator alloys with a giant magnetocaloric effect for magnetic refrigeration

- from similar to 20 to similar to 290 K. *Appl. Phys. Lett.* **70**, 3299–3301 (1997).
31. Hu, F. X., Shen, B. G., Sun, J. R. & Zhang, X. X. Great magnetic entropy change in $\text{La}(\text{Fe}, \text{M})_{13}$ ($\text{M} = \text{Si}, \text{Al}$) with Co doping. *Chin. Phys.* **9**, 550–553 (2000).
 32. Nair, B. et al. Large electrocaloric effects in oxide multilayer capacitors over a wide temperature range. *Nature* **575**, 468–472 (2019).
 33. Li, J. et al. Room-temperature symmetric giant positive and negative electrocaloric effect in $\text{PbMg}_{0.5}\text{W}_{0.5}\text{O}_3$ antiferroelectric ceramic. *Adv. Funct. Mater.* **31**, 2101176 (2021).
 34. Yin, R. et al. Emergent enhanced electrocaloric effect within wide temperature span in laminated composite ceramics. *Adv. Funct. Mater.* **32**, 2108182 (2022).
 35. Griffith, L. D., Mudryk, Y., Slaughter, J. & Pecharsky, V. K. Material-based figure of merit for caloric materials. *J. Appl. Phys.* **123**, 034902 (2018).
 36. Zhou, W. et al. Visualization of ferroelectric domains in thin films of molecular materials using confocal micro-Raman spectroscopy. *Chem. Res. Chin. Univ.* **38**, 1394–1399 (2022).
 37. Silva, R. X. et al. Order-disorder phase transition and molecular dynamics in the hybrid perovskite $[(\text{CH}_3)_3\text{NH}][\text{Mn}(\text{N}_3)_3]$. *Spectrochim. Acta Part A* **289**, 122198 (2023).
 38. Gao, Y. et al. Reversible colossal barocaloric effect dominated by disordering of organic chains in $(\text{CH}_3\text{-(CH}_2\text{)}_{n-1}\text{-NH}_3)_2\text{MnCl}_4$ single crystals. *NPG Asia Mater.* **14**, 34 (2022).
 39. da Silva, R. X. et al. Raman spectroscopy studies on the barocaloric hybrid perovskite $[(\text{CH}_3)_4\text{N}][\text{Cd}(\text{N}_3)_3]$. *Molecules* **25**, 4754 (2020).
 40. Liao, W.-Q. et al. A molecular perovskite solid solution with piezoelectricity stronger than lead zirconate titanate. *Science* **363**, 1206–1210 (2019).
 41. Liao, W.-Q., Tang, Y.-Y., Li, P.-F., You, Y.-M. & Xiong, R.-G. Competitive halogen bond in the molecular ferroelectric with large piezoelectric response. *J. Am. Chem. Soc.* **140**, 3975–3980 (2018).
 42. Sheldrick, G. M. A short history of SHELX. *Acta Crystallogr. A* **64**, 112–122 (2008).
 43. Kresse, G. & Furthmüller, J. Efficient iterative schemes for ab initio total-energy calculations using a plane-wave basis set. *Phys. Rev. B* **54**, 11169 (1996).
 44. Perdew, J. P., Burke, K. & Ernzerhof, M. Generalized gradient approximation made simple. *Phys. Rev. Lett.* **77**, 3865 (1996).
 45. Henkelman, G., Uberuaga, B. P. & Jónsson, H. A climbing image nudged elastic band method for finding saddle points and minimum energy paths. *J. Chem. Phys.* **113**, 9901–9904 (2000).
 46. Singh, G. et al. Electro-caloric effect in $0.45\text{BaZr}_{0.2}\text{Ti}_{0.8}\text{O}_3\text{-}0.55\text{Ba}_{0.7}\text{Ca}_{0.3}\text{TiO}_3$ single crystal. *Appl. Phys. Lett.* **102**, 082902 (2013).
 47. Liu, X. Q., Chen, T. T., Wu, Y. J. & Chen, X. M. Enhanced electrocaloric effects in spark plasma-sintered $\text{Ba}_{0.65}\text{Sr}_{0.35}\text{TiO}_3$ -based ceramics at room temperature. *J. Am. Ceram. Soc.* **96**, 1021–1023 (2013).
 48. Singh, G., Tiwari, V. S. & Gupta, P. K. Electro-caloric effect in $(\text{Ba}_{1-x}\text{Ca}_x)(\text{Zr}_{0.05}\text{Ti}_{0.95})\text{O}_3$: a lead-free ferroelectric material. *Appl. Phys. Lett.* **103**, 202903 (2013).
 49. Kaddoussi, H. et al. Room temperature electro-caloric effect in lead-free $\text{Ba}(\text{Zr}_{0.1}\text{Ti}_{0.9})_{1-x}\text{Sn}_x\text{O}_3$ ($x=0, x=0.075$) ceramics. *Solid State Commun.* **201**, 64–67 (2015).
 50. Qian, X.-S. et al. Giant electrocaloric response over a broad temperature range in modified BaTiO_3 ceramics. *Adv. Funct. Mater.* **24**, 1300–1305 (2014).
 51. Bai, Y. et al. The giant electrocaloric effect and high effective cooling power near room temperature for BaTiO_3 thick film. *J. Appl. Phys.* **110**, 094103 (2011).
 52. Kar-Narayan, S. & Mathur, N. D. Direct and indirect electrocaloric measurements using multilayer capacitors. *J. Phys. D Appl. Phys.* **43**, 032002 (2010).
 53. Luo, Z. et al. Enhanced electrocaloric effect in lead-free $\text{BaTi}_{1-x}\text{Sn}_x\text{O}_3$ ceramics near room temperature. *Appl. Phys. Lett.* **105**, 102904 (2014).
 54. Shebanov, L. A., Birks, E. H. & Borman, K. J. X-ray studies of electrocaloric lead-scandium tantalate ordered solid-solutions. *Ferroelectrics* **90**, 165–172 (1989).
 55. Birks, E. H. The electrocaloric effect in $\text{PB}(\text{SC}_{0.5}\text{NB}_{0.5})\text{O}_3$ ceramic. *Phys. Status Solidi a Appl. Res.* **94**, 523–527 (1986).
 56. Peng, B., Fan, H. & Zhang, Q. A giant electrocaloric effect in nanoscale antiferroelectric and ferroelectric phases coexisting in a relaxor $\text{Pb}_{0.8}\text{Ba}_{0.2}\text{ZrO}_3$ Thin Film At Room Temperature. *Adv. Funct. Mater.* **23**, 2987–2992 (2013).
 57. Tuttle, B. A. & Payne, D. A. The effects of microstructure on the electrocaloric properties of $\text{PB}(\text{ZR}, \text{SN}, \text{TI})\text{O}_3$ ceramics. *Ferroelectrics* **37**, 603–606 (1981).
 58. Rozic, B. et al. Influence of the critical point on the electrocaloric response of relaxor ferroelectrics. *J. Appl. Phys.* **110**, 064118 (2011).
 59. Hao, X. & Zhai, J. Electric-field tunable electrocaloric effects from phase transition between antiferroelectric and ferroelectric phase. *Appl. Phys. Lett.* **104**, 022902 (2014).
 60. Li, X. et al. Giant electrocaloric effect in ferroelectric poly(vinylidene fluoride-trifluoroethylene) copolymers near a first-order ferroelectric transition. *Appl. Phys. Lett.* **101**, 132903 (2012).
 61. Li, X. et al. Tunable temperature dependence of electrocaloric effect in ferroelectric relaxor poly(vinylidene fluoride-trifluoroethylene-chlorofluoroethylene) terpolymer. *Appl. Phys. Lett.* **99**, 052907 (2011).
 62. Qian, J. et al. Interfacial coupling boosts giant electrocaloric effects in relaxor polymer nanocomposites: in situ characterization and phase-field simulation. *Adv. Mater.* **31**, 1801949 (2019).
 63. Zhang, G. et al. Colossal room-temperature electrocaloric effect in ferroelectric polymer nanocomposites using nanostructured barium strontium titanates. *ACS Nano* **9**, 7164–7174 (2015).
 64. Lu, S. G. et al. Organic and inorganic relaxor ferroelectrics with giant electrocaloric effect. *Appl. Phys. Lett.* **97**, 162904 (2010).
 65. Chukka, R. et al. Enhanced cooling capacities of ferroelectric materials at morphotropic phase boundaries. *Appl. Phys. Lett.* **98**, 242902 (2011).
 66. Luo, L., Dietze, M., Solterbeck, C.-H., Es-Souni, M. & Luo, H. Orientation and phase transition dependence of the electrocaloric effect in $0.71\text{PbMg}_{1/3}\text{Nb}_{2/3}\text{O}_3\text{-}0.29\text{PbTiO}_3$ single crystal. *Appl. Phys. Lett.* **101**, 062907 (2012).
 67. Sebald, G. et al. Electrocaloric and pyroelectric properties of $0.75\text{Pb}(\text{Mg}_{1/3}\text{Nb}_{2/3})\text{O}_3\text{-}0.25\text{PbTiO}_3$ single crystals. *J. Appl. Phys.* **100**, 124112 (2006).
 68. Liu, S. B. & Li, Y. Q. Research on the electrocaloric effect of PMN/PT solid solution for ferroelectrics MEMS microcooler. *Mater. Sci. Eng. B Solid State Mater. Adv. Technol.* **113**, 46–49 (2004).
 69. Xiao, D. Q. et al. Electrocaloric properties of $(1-x)\text{Pb}(\text{Mg}_{1/3}\text{Nb}_{2/3})\text{O}_3\text{-}x\text{PbTiO}_3$ ferroelectric ceramics near room temperature. *Mater. Chem. Phys.* **57**, 182–185 (1998).
 70. Rozic, B. et al. Direct measurements of the giant electrocaloric effect in soft and solid ferroelectric materials. *Ferroelectrics* **405**, 26–31 (2010).
 71. Luo, L. et al. Pyroelectric and electrocaloric effect of (111)-oriented $0.9\text{PMN}\text{-}0.1\text{PT}$ single crystal. *J. Alloy. Compd.* **509**, 8149–8152 (2011).
 72. Mischenko, A. S., Zhang, Q., Whatmore, R. W., Scott, J. F. & Mathur, N. D. Giant electrocaloric effect in the thin film relaxor ferroelectric $0.9\text{PbMg}_{1/3}\text{Nb}_{2/3}\text{O}_3\text{-}0.1\text{PbTiO}_3$ near room temperature. *Appl. Phys. Lett.* **89**, 242912 (2006).
 73. Cao, W. P. et al. Enhanced electrocaloric effect in lead-free NBT-based ceramics. *Ceram. Int.* **40**, 9273–9278 (2014).
 74. Bai, Y., Zheng, G.-P. & Shi, S.-Q. Abnormal electrocaloric effect of $\text{Na}_{0.5}\text{Bi}_{0.5}\text{TiO}_3\text{-BaTiO}_3$ lead-free ferroelectric ceramics above room temperature. *Mater. Res. Bull.* **46**, 1866–1869 (2011).

Acknowledgements

This work was supported by the National Key Research and Development Program of China (Grant Nos. 2020YFA0711500 (J.W. and Y.Y.), 2023YFA1406003 (F.H.), 2021YFB3501202 (F.H.)), the National Natural Sciences Foundation of China (Grant Nos. 52088101 (B.S.), 92263202 (F.H.), U23A20550 (F.H.), 22361132534 (J.W. and F.H.)), and the Strategic Priority Research Program (B) of the Chinese Academy of Sciences (XDB33030200 (B.S. and F.H.)). A portion of this work was carried out at the Synergetic Extreme Condition User Facility (SECUF). J.Y.L. and V.F. acknowledge the support of AEI/FEDER-UE (grants PID2019-105720RB-I00 (J.Y.L. and V.F.) and PID2023-146047OB-I00 (J.Y.L. and V.F.) from AEI/10.13039/501100011033), and of the Chinese Academy of Sciences President's International Fellowship Initiative (PIFI) for visiting scientists (Grants No. 2024VMC0006 (J.Y.L.), 2024VMA0021 (V.F.)). J.Y.L. acknowledges an EMERGIA 2021 Fellowship (EMC21_00418 (J.Y.L.)) from Junta de Andalucía.

Author contributions

F.H., V.F., and B.S. designed the research. Y.L. performed the measurement of P-E loops. Y.L., S.J., and Y.B. analyzed the P-E loop results. Y.L. performed DSC measurements. Y.L., J.W., and F.H. analyzed DSC results. Y.L. collected Raman Spectra. Y.L., J.W., and F.H. analyzed the Spectra. C.C. synthesized the sample. Y.L., C.C., and X.L. prepared samples for measurements. C.C. performed the SC-XRD measurements. C.C., Y.L., and S.J. analyzed the SC-XRD results. Z.L., X.M., and Y.Y. performed DFT calculations. Z.L., Y.L., and Y.Y. analyzed the DFT results. Y.H., Y.L., Y.G., and Y.K. measured the heat capacity. Y.L. drafted the paper, and J.W., F.H., and V.F. finalized it with input from all coauthors. B.W., Z.W., J.Z., M.H., Y.C., J.S., and T.Z. contributed to discussing and revising the paper. J.W., F.H., V.F., J.Y.L., and B.S. supervised the research and secured the funds.

Competing interests

The authors declare no competing interests.

Additional information

Supplementary information The online version contains supplementary material available at <https://doi.org/10.1038/s41467-025-58914-z>.

Correspondence and requests for materials should be addressed to Jing Wang, Shifeng Jin, Yurong Yang, Victorino Franco or Fengxia Hu.

Peer review information *Nature Communications* thanks Xitao Liu and the other, anonymous, reviewer(s) for their contribution to the peer review of this work. A peer review file is available.

Reprints and permissions information is available at <http://www.nature.com/reprints>

Publisher's note Springer Nature remains neutral with regard to jurisdictional claims in published maps and institutional affiliations.

Open Access This article is licensed under a Creative Commons Attribution-NonCommercial-NoDerivatives 4.0 International License, which permits any non-commercial use, sharing, distribution and reproduction in any medium or format, as long as you give appropriate credit to the original author(s) and the source, provide a link to the Creative Commons licence, and indicate if you modified the licensed material. You do not have permission under this licence to share adapted material derived from this article or parts of it. The images or other third party material in this article are included in the article's Creative Commons licence, unless indicated otherwise in a credit line to the material. If material is not included in the article's Creative Commons licence and your intended use is not permitted by statutory regulation or exceeds the permitted use, you will need to obtain permission directly from the copyright holder. To view a copy of this licence, visit <http://creativecommons.org/licenses/by-nc-nd/4.0/>.

© The Author(s) 2025